Journal of
Applied Crystallography
ISSN 0021-8898
Editor: **Anke R. Kaysser-Pyzalla**

Angle calculations for a (2+3)-type diffractometer: focus on area detectors

Christian M. Schlepütz, Simon O. Mariager, Stephan A. Pauli, Robert Feidenhans'l and Philip R. Willmott

J. Appl. Cryst. (2011). **44**, 73–83

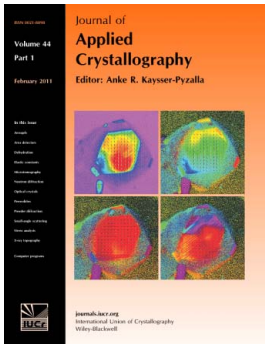

Journal of
Applied Crystallography
ISSN 0021-8898

Received 18 June 2010
Accepted 23 November 2010

Angle calculations for a (2+3)-type diffractometer: focus on area detectors

Christian M. Schlepütz,[a]*‡ Simon O. Mariager,[b] Stephan A. Pauli,[a] Robert Feidenhans'l[b] and Philip R. Willmott[a]

[a]Swiss Light Source, Paul Scherrer Institut, CH-5232 Villigen-PSI, Switzerland, and [b]Niels Bohr Institute, University of Copenhagen, Universitetsparken 5, 2100 Copenhagen, Denmark. Correspondence e-mail: cschlep@umich.edu

Angle calculations for a (2+3)-type diffractometer are presented with comprehensive derivations for both cases of either a vertical or horizontal sample configuration. This work focuses on some particular aspects of using area detectors in surface X-ray diffraction, namely the role of the detector rotation and the direct conversion of the angle-resolved diffraction signal recorded by the detector into a two-dimensional slice through reciprocal space.

1. Introduction

Over the past few decades, a number of different diffractometer types have been developed to study single crystals using neutrons or X-rays in general and single-crystal surfaces and thin-film systems in particular; the choice of a specific geometry is largely based on the required experimental conditions. A brief overview of the different types used in surface X-ray diffraction (SXRD), their relative merits and drawbacks, and their classification has been given by Bunk & Nielsen (2004).

With very few exceptions, modern surface diffractometers can be grouped into two categories. The z-axis-type instruments have coupled detector and sample circles in conjunction with a rotation stage for the entire instrument (Bloch, 1985; Lohmeier & Vlieg, 1993). The vertical-axis diffractometers, on the other hand, feature completely independent detector and sample circles. The (2+2)-type diffractometer (Hung, 1992; Evans-Lutterodt & Tang, 1995; Renaud *et al.*, 1995) provides two sample and two detector rotations. Adding an additional two degrees of freedom for the sample orientation, the (4+2)-type instrument (Takahasi & Mizuki, 1998; You, 1999) provides more flexibility and versatility, albeit at the cost of mechanical complexity. In contrast, the (2+3)-type diffractometer (Vlieg, 1998) introduces an additional detector rotation to the (2+2) configuration, which combines many of the advantages of the z-axis- and (2+2)-type geometries.

In this article, we present a comprehensive derivation of the angle calculations as implemented for the Newport (2+3)-type diffractometer of the Materials Science Beamline X04SA at the Swiss Light Source (SLS), including both the vertical and the horizontal sample configurations.

Based on these calculations, we then focus on some particular aspects regarding the use of area detectors in SXRD. Firstly, the role of the detector rotation is discussed, specifically in view of using area detectors in a stationary mode (Specht & Walker, 1993; Vlieg, 1997; Schlepütz *et al.*, 2005), where the total diffracted signal and background are captured in a single exposure. A new detector rotation mode is introduced which significantly facilitates the intensity integration and efficiently reduces scattering background not originating from the sample position. Secondly, the conversion from pixel coordinates to reciprocal-space positions is discussed in detail. The angle-resolved scattering pattern on the detector is transformed into a curved two-dimensional slice through reciprocal space. By collecting many such slices, three-dimensional reciprocal-space maps can be reconstructed from a single scan (Schmidbauer *et al.*, 2008; Mariager, Lauridsen *et al.*, 2009). Optimal sampling of reciprocal space is achieved by scanning along the reciprocal-space direction normal to the surface of the Ewald sphere ($\mathbf{k}_{\rm out}$).

Although all calculations in this article are performed specifically for the (2+3)-type diffractometer, the presented concepts are generally applicable to any diffractometer geometry.

2. Experimental setup

2.1. The (2+3)-type surface diffractometer

The Newport (2+3) circle diffractometer is shown schematically in Fig. 1. The naming conventions for the instrument circles follow those used by Vlieg (1998). The diffractometer provides two degrees of freedom for the sample motion and three for the detector. The γ and δ circles are used to position the detector in the direction of the diffracted X-ray beam, $\mathbf{k}_{\rm out}$, while the ν-axis rotation allows the detector and the slit system attached to it to turn around $\mathbf{k}_{\rm out}$.

For a (2+3)-type instrument, the two sample circles are fully decoupled from the detector circles. This allows for two alternative modes of operation, mounting the sample either in the vertical or in the horizontal scattering geometry. In the vertical geometry (blue in the electronic version of the paper,

‡ Present address: Department of Physics, University of Michigan, 450 Church Street, Ann Arbor, MI 48109-1040, USA.

dark shading in the print version, see Fig. 1), the sample surface plane is vertical, and hence its surface normal direction lies in the horizontal plane. The grazing-incidence angle of the synchrotron beam onto the surface is adjusted using the α circle, while ω_v provides the azimuthal sample rotation around the surface normal. When using the horizontal geometry (red in the electronic version of the paper, light shading in the print version), the sample surface is approximately horizontal with the surface normal pointing upwards. Here, φ and ω_h determine the grazing angle and azimuthal orientation, respectively. (In this geometry, the α circle is only used to align the ω_h axis with the δ axis, and is kept fixed during the rest of the experiment.) Both geometries have their relative merits and drawbacks with regard to exploiting the beam polarization, maximizing the experimental resolution or the use of heavy sample chambers. Which mode should be used therefore depends on the demands of the experiment.

Six additional sample degrees of freedom (three translations and three rotations) are provided by a hexapod, mounted onto the ω_v (vertical) or φ (horizontal) sample circle. The three linear motions are used to bring the sample centre into coincidence with the diffractometer centre. The sample surface normal is accurately aligned with the diffractometer's azimuthal sample rotation axis (ω_v in the vertical and φ in the horizontal geometry) using the hexapod rotations. All angle calculations require this coincidence of sample surface normal and azimuthal rotation axis, so once the sample is accurately aligned, the hexapod positions are fixed for the rest of the experiment.

Of particular note are the two different laboratory coordinate frames for the horizontal and vertical scattering geometries: they have both been chosen such that the incoming synchrotron beam points in the positive y direction and the sample surface normal at 0° grazing-incidence angle lies along the z axis.

2.2. The PILATUS 100K pixel detector

The standard detector used in the setup is a PILATUS 100K single-module pixel detector. Its characteristics have been described in detail elsewhere (Schlepütz *et al.*, 2005; Bergamaschi *et al.*, 2007; Kraft, Bergamaschi, Brönnimann, Dinapoli, Eikenberry, Graafsma *et al.*, 2009; Kraft, Bergamaschi, Broennimann, Dinapoli, Eikenberry, Henrich *et al.*, 2009; Sobott *et al.*, 2009). Briefly, it is an X-ray single-photon-counting hybrid pixel detector with an energy range of 3–30 keV and a dynamic range of $2^{20} \simeq 10^6$ pixel^{-1}. The module consists of 487 × 195 pixels with a pitch of 172 × 172 µm each, resulting in a total active area of 83.8 × 33.5 mm. The short readout time of 2.7 ms allows for frame rates of up to 300 Hz, and a variable high-pass energy threshold with a bandwidth of *circa* 500 eV can be used to suppress unwanted inelastic scattering signals (*e.g.* fluorescence background).

The detector is mounted on the ν axis at a distance $R = 1140.8$ mm from the centre of the diffractometer, thus subtending an angular range of $4.205 \times 1.684°$ ($0.0086°$ pixel^{-1}). A set of guard slits attached to the ν axis can be brought close to the sample to limit the detector's field of view. There are currently no detector slits directly in front of the pixel detector since the slitting operation can be performed digitally by selecting corresponding regions of interest in the detector images.

3. Angle calculations

Angle calculations for the (2+3)-type diffractometer are presented for both the vertical and the horizontal sample geometry. Because the detector rotation around the ν axis does not affect the direction of the observed scattering vector for the particular point of the detector lying on the rotation axis, it does not enter the angle calculations directly. For this reason, the derivations are essentially identical to those published by Evans-Lutterodt & Tang (1995) for the (2+2) surface diffractometer in the vertical geometry, but will be reproduced here for completeness, using the appropriate rotations for our particular setup. These results will be essential to discuss a new mode for the detector rotation relevant when using an area detector in §4, and to calculate the direct relation between pixel coordinates and reciprocal-space positions to obtain reciprocal-space maps (RSMs) from a single detector image in §5.

3.1. Basic equations

Consider a crystal lattice defined by three lattice vectors $\mathbf{a}_i$ ($i = 1, 2, 3$) of length $a_i = |\mathbf{a}_i|$, and the three lattice angles α_i between them. The corresponding reciprocal lattice is spanned

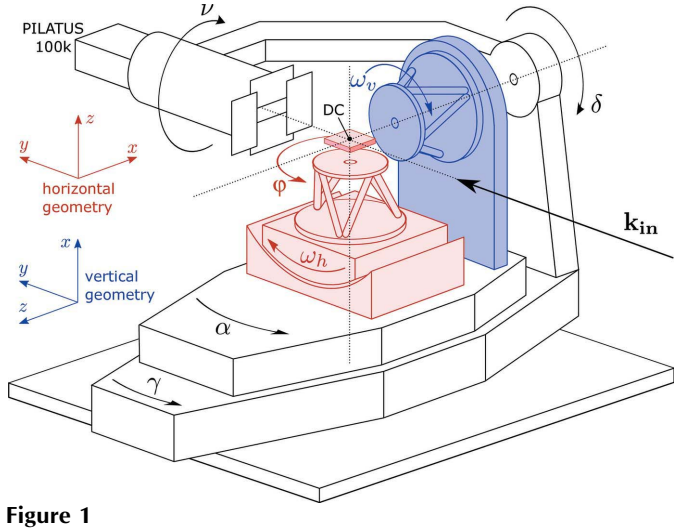

Figure 1
Schematic of the Newport (2+3) circle diffractometer with all circles shown at their zero positions. The two sample circles can be configured in one of two alternative modes. (i) In the 'vertical geometry' (blue, or dark shading in the print version of the paper), the sample surface lies in a vertical plane, hence the surface normal is horizontal. Here, ω_v and α provide the azimuthal and polar degrees of freedom, respectively. (ii) In the 'horizontal geometry' (red, or light shading in the print version of the paper), the sample surface is kept approximately horizontal, while the surface normal points upwards. The azimuthal and polar rotations are now provided by the φ and ω_h circles. The detector has three degrees of freedom: γ and δ are used to position the detector in the direction of the diffracted X-ray beam, while the ν axis provides a rotation of the detector around this direction. All rotation axes intersect at the diffractometer centre (DC).

by the vectors $\mathbf{b}_i$ with angles β_i. Any vector $\mathbf{H}$ in reciprocal space can be written as

$$\mathbf{H} = h\mathbf{b}_1 + k\mathbf{b}_2 + l\mathbf{b}_3, \tag{1}$$

with reciprocal-space coordinates *hkl*.

To obtain a description independent of a particular crystal lattice, it is necessary to convert the reciprocal-space vector $\mathbf{H}$ from the crystal or surface coordinate system to an orthonormal coordinate system attached to the crystal lattice (Busing & Levy, 1967). Conventionally, the x axis of this Cartesian coordinate system is chosen along $\mathbf{b}_1$, y inside the plane of $\mathbf{b}_1$ and $\mathbf{b}_2$, and z perpendicular to that plane. This leads to the transformation

$$\mathbf{H}_\mathrm{c} = B\,\mathbf{H}, \tag{2}$$

where the subscript 'c' denotes the Cartesian coordinate system, and B is given by Busing & Levy (1967):

$$B = \begin{pmatrix} b_1 & b_2\cos\beta_3 & b_3\cos\beta_2 \\ 0 & b_2\sin\beta_3 & -b_3\sin\beta_2\cos\alpha_1 \\ 0 & 0 & 2\pi/a_3 \end{pmatrix}. \tag{3}$$

Note that this formula differs from the original by Busing & Levy (1967) by a factor of 2π in $B(3, 3)$. This depends on the particular convention to define the reciprocal-lattice vectors, where we use the 'physics' definition,

$$a_i b_i = 2\pi;\ a_i b_j = 0 \qquad \forall\, i, j \in 1, 2, 3, i \neq j, \tag{4}$$

rather than the 'crystallographic' definition, where $a_i b_i = 1$.

This crystal Cartesian coordinate system can be related to another orthonormal coordinate system, the ω system (φ system), which has its z axis rigidly aligned with the diffractometer's azimuthal sample rotation axis ω_v (φ) in the vertical (horizontal) geometry through an additional rotation of the crystal, represented by the orthogonal rotation matrix U, such that

$$\mathbf{H}_{\varphi/\omega} = U\,\mathbf{H}_\mathrm{c} = UB\,\mathbf{H}. \tag{5}$$

U is the so-called orientation matrix and depends on the way the crystal is oriented on the diffractometer. U is not known *a priori*, but can be determined through the measured angular positions of two known reflections (Busing & Levy, 1967; Shoemaker & Bassi, 1970). A very practical and common alternative which may yield a more stable orientation is to apply a linear least-squares fit for the entire UB matrix using more than three measured reflections with known *hkl* indices (Busing & Levy, 1967). Note, however, that this method will also change the lattice constants and angles, invariably resulting in a slightly distorted, triclinic lattice. Various ways of constraining some of these parameters to known values (*i.e.* the lattice angles for a known crystal symmetry) generally lead to nonlinear optimization problems which need to be solved iteratively (Busing & Levy, 1967; Shoemaker & Bassi, 1970; Shoemaker, 1970; Ralph & Finger, 1982). A further option is to assume that the unit cell remains unchanged, and only the three orientational degrees of freedom in U need to be refined. Using standard (3×3) rotation matrix notation, this results in a nonlinear set of equations. However, by employing quaternion algebra, this problem is reduced to a linear least-squares fit again which can be solved analytically (Mackay, 1984; Clegg, 1984) for two or more known reflections.

With all diffractometer positions set to zero, the $\mathbf{H}_{\varphi/\omega}$-axis system coincides with the corresponding laboratory frame of reference $\{x, y, z\}$, shown in Fig. 1.

Given our choice of laboratory coordinates (§2.1), and using units of $2\pi/\lambda$, where λ is the X-ray wavelength, the incoming wavevector has a magnitude equal to unity and can be expressed as

$$\mathbf{k}_\mathrm{in,lab} = \begin{pmatrix} 0 \\ 1 \\ 0 \end{pmatrix}. \tag{6}$$

The diffraction condition is then given by

$$\mathbf{H}_\mathrm{lab} = \mathbf{k}_\mathrm{out,lab} - \mathbf{k}_\mathrm{in,lab} = \begin{pmatrix} X \\ Y \\ Z \end{pmatrix}. \tag{7}$$

(X, Y, Z) is the momentum transfer in the laboratory frame $\{x, y, z\}$. Since we are concerned here with elastic scattering processes, the magnitude of the outgoing wavevector is equal to that of the incoming wavevector, and its direction is given by the position of the detector, defined by the detector circles γ and δ.

The effect of a rotation of one of the diffractometer circles is described through a rotation matrix, defined in the appropriate coordinate system. Usually it is most convenient to use the laboratory frame of reference to express the rotations, since the rotation axes are normally aligned with one of the coordinate axes. Note, however, that under these circumstances, the order of applying the rotations is important for those circles that are mechanically coupled, as spatial rotations are non-commutative in general. Consider, as an example, a rotation of the detector arm using the γ and δ circles (see Fig. 1). By rotating the γ circle, the δ axis is no longer oriented along the laboratory's z axis and hence the form of the rotation matrix needs to be modified. Applying the δ rotation first, however, has no effect on the orientation of the γ axis, and both rotations can be described in the laboratory frame of reference.

3.2. Vertical geometry

The relevant rotation matrices for the vertical geometry are the following:

$$\Gamma = \mathcal{R}_x(\gamma) = \begin{pmatrix} 1 & 0 & 0 \\ 0 & \cos\gamma & -\sin\gamma \\ 0 & \sin\gamma & \cos\gamma \end{pmatrix}; \tag{8}$$

$$A = \mathcal{R}_x(\alpha) = \begin{pmatrix} 1 & 0 & 0 \\ 0 & \cos\alpha & -\sin\alpha \\ 0 & \sin\alpha & \cos\alpha \end{pmatrix}; \tag{9}$$

$$\Delta = \mathcal{R}_z^-(\delta) = \begin{pmatrix} \cos\delta & \sin\delta & 0 \\ -\sin\delta & \cos\delta & 0 \\ 0 & 0 & 1 \end{pmatrix}; \quad (10)$$

$$\Omega_v = \mathcal{R}_z^-(\omega_v) = \begin{pmatrix} \cos\omega_v & \sin\omega_v & 0 \\ -\sin\omega_v & \cos\omega_v & 0 \\ 0 & 0 & 1 \end{pmatrix}. \quad (11)$$

Note that Δ and Ω_v represent *left-handed* rotations around the laboratory z axis (indicated by the minus sign in $\mathcal{R}_z^-$).

Writing **I** for the identity matrix, the diffraction condition in equation (7) can now be expressed in terms of these rotations:

$$\mathbf{H}_{lab} = \mathbf{k}_{out} - \mathbf{k}_{in} = (\Gamma \times \Delta - \mathbf{I}) \begin{pmatrix} 0 \\ 1 \\ 0 \end{pmatrix}, \quad (12)$$

yielding

$$\begin{pmatrix} X \\ Y \\ Z \end{pmatrix} = \begin{pmatrix} \sin\delta \\ \cos\gamma\,\cos\delta - 1 \\ \sin\gamma\,\cos\delta \end{pmatrix}. \quad (13)$$

The corresponding scattering vector $\mathbf{H}_\omega$ in the ω system is determined by the orientation of the sample stage

$$\mathbf{H}_\omega = \begin{pmatrix} h_\omega \\ k_\omega \\ l_\omega \end{pmatrix} = \Omega_v^{-1} A^{-1} \begin{pmatrix} X \\ Y \\ Z \end{pmatrix}. \quad (14)$$

Multiplying out, we obtain

$$\begin{pmatrix} h_\omega \\ k_\omega \\ l_\omega \end{pmatrix} = \begin{bmatrix} \cos\omega_v X - \sin\omega_v(\cos\alpha\, Y + \sin\alpha\, Z) \\ \sin\omega_v X + \cos\omega_v(\cos\alpha\, Y + \sin\alpha\, Z) \\ -\sin\alpha\, Y + \cos\alpha\, Z \end{bmatrix}. \quad (15)$$

Consider Fig. 2. The momentum transfer perpendicular to the sample surface, $\mathbf{q}_\perp$, is equal to l_ω in the ω system, and in units of $2\pi/\lambda$, it is given by

$$l_\omega = \sin\beta_{in} + \sin\beta_{out}. \quad (16)$$

On the other hand, combining equations (13) and (15), we see also that

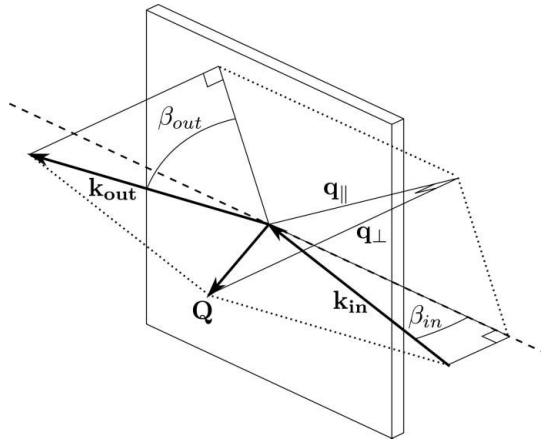

Figure 2
Scattering triangle in the vertical geometry. The magnitude of the perpendicular momentum transfer, $\mathbf{q}_\perp$, is equal to $|\mathbf{k}_{in}|\sin\beta_{in} + |\mathbf{k}_{out}|\sin\beta_{out}$.

$$\begin{aligned} l_\omega &= -\sin\alpha\, Y + \cos\alpha\, Z \\ &= -\sin\alpha\,(\cos\gamma\,\cos\delta - 1) + \cos\alpha\sin\gamma\cos\delta \\ &= \cos\delta\,(\sin\gamma\,\cos\alpha - \cos\gamma\,\sin\alpha) + \sin\alpha \\ &= \cos\delta\,\sin(\gamma - \alpha) + \sin\alpha. \end{aligned} \quad (17)$$

Since $\beta_{in} = \alpha$, it follows that

$$\cos\delta\,\sin(\gamma - \alpha) = \sin(\beta_{out}). \quad (18)$$

The (squared) magnitude of the in-plane component of $\mathbf{H}_\omega$ should not depend on ω_v, as this rotation is always normal to the crystal surface. Combining equations (13) and (15) yields

$$\begin{aligned} h_\omega^2 + k_\omega^2 &= [\cos\omega_v X - \sin\omega_v(\cos\alpha Y + \sin\alpha Z)]^2 \\ &\quad + [\sin\omega_v X + \cos\omega_v(\cos\alpha Y + \sin\alpha Z)]^2 \\ &= X^2 + (\cos\alpha Y + \sin\alpha Z)^2, \end{aligned} \quad (19)$$

which is indeed independent of ω_v.

The magnitude of $\mathbf{H}_\omega$ is equal to that of $\mathbf{H}_{lab}$ and also independent of ω_v. From equation (13), we obtain

$$\begin{aligned} h_\omega^2 + k_\omega^2 + l_\omega^2 &= X^2 + Y^2 + Z^2 \\ &= (\sin\delta)^2 + (\cos\gamma\cos\delta - 1)^2 + (\sin\gamma\cos\delta)^2 \\ &= 2(1 - \cos\gamma\cos\delta) = -2Y, \end{aligned} \quad (20)$$

which yields

$$Y = -(1/2)(h_\omega^2 + k_\omega^2 + l_\omega^2). \quad (21)$$

From equation (18), we know that

$$\begin{aligned} \sin\beta_{out} &= \cos\delta\sin(\gamma - \alpha) = \cos\delta(\sin\gamma\,\cos\alpha - \cos\gamma\,\sin\alpha) \\ &= \cos\alpha Z - \sin\alpha(Y + 1). \end{aligned} \quad (22)$$

We rearrange this to obtain

$$Z = [\sin\beta_{out} + \sin\alpha(Y + 1)]/\cos\alpha. \quad (23)$$

Finally, we can solve equation (19) for X as a function of the known Y and Z:

$$X = \pm[h_\omega^2 + k_\omega^2 - (\cos\alpha Y + \sin\alpha Z)^2]^{1/2}. \quad (24)$$

The scattering vector components X, Y and Z in the laboratory frame of reference have now been expressed only in terms of h_ω, k_ω and l_ω [the momentum transfer components in the ω system, which are related to the desired components h, k and l of **H** through equation (5)] and β_{in} and β_{out}, which are still free variables.

We now determine the diffractometer angles α, γ, δ and ω_v in terms of h_ω, k_ω and l_ω, and X, Y and Z (which, we have just stated, can themselves be expressed in terms of h_ω, k_ω and l_ω, and β_{in} and β_{out}). From equation (13), we directly obtain

$$\sin\delta = X. \quad (25)$$

Here, we choose the positive solution for X from equation (24) to make the diffractometer move to positive values of δ.

The expression for γ is derived in the following way:

$$\tan\gamma = \frac{\sin\gamma}{\cos\gamma} = \frac{\sin\gamma\cos\delta}{\cos\gamma\cos\delta} = \frac{\sin\gamma\cos\delta}{(\cos\gamma\cos\delta - 1) + 1} \quad (26)$$

$$= \frac{Z}{Y+1}. \tag{27}$$

In order to obtain an expression for ω_v, we first define

$$(\cos\beta_{in} Y + \sin\beta_{in} Z) \equiv M, \tag{28}$$

which we substitute into equation (15) to obtain

$$\begin{aligned} h_\omega &= \cos\omega_v X - \sin\omega_v M \\ \Rightarrow \cos\omega_v &= \frac{h_\omega + \sin\omega_v M}{X} \end{aligned} \tag{29}$$

and

$$\begin{aligned} k_\omega &= \sin\omega_v X + \cos\omega_v M \\ \Rightarrow \sin\omega_v &= \frac{k_\omega - \cos\omega_v M}{X}, \end{aligned} \tag{30}$$

and combining these two expressions, we obtain

$$\begin{aligned} \sin\omega_v &= \frac{k_\omega - [(h_\omega + \sin\omega_v M)/X]M}{X} \\ &= \frac{k_\omega}{X} - \frac{h_\omega M}{X^2} - \frac{\sin\omega_v M^2}{X^2} \\ \Rightarrow \sin\omega_v \left(1 + \frac{M^2}{X^2}\right) &= \frac{k_\omega X}{X^2} - \frac{h_\omega M}{X^2} \\ \Rightarrow \sin\omega_v &= \frac{k_\omega X - h_\omega M}{X^2 + M^2}. \end{aligned} \tag{31}$$

Because ω_v can assume values between +180 and −180°, the sine of the desired angle alone does not suffice to determine the angle unambiguously. So we also solve for $\cos\omega_v$ by inserting equation (30) into equation (29):

$$\cos\omega_v = \frac{h_\omega X + k_\omega M}{X^2 + M^2}. \tag{32}$$

Combining equations (31) and (32) yields

$$\tan\omega_v = \frac{k_\omega X - h_\omega M}{h_\omega X + k_\omega M}, \tag{33}$$

which, if we use a quadrant-sensitive arctangent function (such as `atan2` in standard C), unambiguously determines ω_v. Finally,

$$\sin\alpha = \sin\beta_{in}. \tag{34}$$

To calculate the diffractometer angles, we need to impose one final constraint to determine β_{in} and β_{out}. We know from equation (16) that

$$l_\omega = \sin\beta_{in} + \sin\beta_{out}. \tag{35}$$

The three commonly used constraints on β_{in} and β_{out} are the following (though others could be used as well):

(*a*) Fixing the incoming angle, $\beta_{in} = \alpha$, yields

$$\begin{aligned} \sin\alpha &= \sin\beta_{in}, \\ \sin\beta_{out} &= l_\omega - \sin\alpha. \end{aligned} \tag{36}$$

(*b*) For a fixed outgoing angle β_{out}, we obtain

$$\sin\alpha = l_\omega - \sin\beta_{out}. \tag{37}$$

(*c*) Requiring the incoming and outgoing angles to be equal, $\beta_{in} = \beta_{out}$, we find

$$\sin\alpha = \sin\beta_{out} = l_\omega/2. \tag{38}$$

Inserting the appropriate constraints on β_{in} and β_{out} from equations (36), (37) or (38) into our expression for X, Y and Z [equations (24), (21) and (23), respectively] and then using these to evaluate equations (25), (27), (31) and (34), we are then able to compute δ, γ, ω_v and α, respectively.

3.3. Horizontal geometry

The angle calculations for the horizontal geometry are completely analogous to the vertical case. Here, the relevant rotation matrices with respect to the horizontal geometry coordinate system (see Fig. 1) are the following:

$$\Gamma = \mathcal{R}_z(\gamma) = \begin{pmatrix} \cos\gamma & -\sin\gamma & 0 \\ \sin\gamma & \cos\gamma & 0 \\ 0 & 0 & 1 \end{pmatrix}; \tag{39}$$

$$\Delta = \mathcal{R}_x(\delta) = \begin{pmatrix} 1 & 0 & 0 \\ 0 & \cos\delta & -\sin\delta \\ 0 & \sin\delta & \cos\delta \end{pmatrix}; \tag{40}$$

$$\Phi = \mathcal{R}_z(\varphi) = \begin{pmatrix} \cos\varphi & -\sin\varphi & 0 \\ \sin\varphi & \cos\varphi & 0 \\ 0 & 0 & 1 \end{pmatrix}; \tag{41}$$

$$\Omega_h = \mathcal{R}_x(\omega_h) = \begin{pmatrix} 1 & 0 & 0 \\ 0 & \cos\omega_h & -\sin\omega_h \\ 0 & \sin\omega_h & \cos\omega_h \end{pmatrix}. \tag{42}$$

The diffraction condition [*cf.* equation (7)] then becomes

$$\begin{pmatrix} X \\ Y \\ Z \end{pmatrix} = (\Gamma \times \Delta - \mathbf{I}) \begin{pmatrix} 0 \\ 1 \\ 0 \end{pmatrix} = \begin{pmatrix} -\sin\gamma\cos\delta \\ \cos\gamma\cos\delta - 1 \\ \sin\delta \end{pmatrix}, \tag{43}$$

and transforming this into the φ system yields

$$\begin{aligned} \mathbf{H}_\varphi = \begin{pmatrix} h_\varphi \\ k_\varphi \\ l_\varphi \end{pmatrix} &= \Phi^{-1} \times \Omega_h^{-1} \begin{pmatrix} X \\ Y \\ Z \end{pmatrix} \\ &= \begin{bmatrix} \sin\varphi(\cos\omega_h Y + \sin\omega_h Z) + \cos\varphi X \\ \cos\varphi(\cos\omega_h Y + \sin\omega_h Z) - \sin\varphi X \\ \cos\omega_h Z - \sin\omega_h Y \end{bmatrix} \end{aligned} \tag{44}$$

Remembering that the incoming angle in the horizontal geometry is given by $\beta_{in} = \omega_h$, we can now construct the expressions for X, Y and Z:

$$\begin{aligned} h_\varphi^2 + k_\varphi^2 + l_\varphi^2 = X^2 + Y^2 + Z^2 &= -2Y \\ \Rightarrow Y &= -(h_\varphi^2 + k_\varphi^2 + l_\varphi^2)/2. \end{aligned} \tag{45}$$

Using Y, we first obtain Z:

$$\begin{aligned} l_\varphi &= \sin\beta_{in} + \sin\beta_{out} \\ &= \sin\omega_h + \sin\delta\cos\omega_h - \cos\delta\sin\omega_h\cos\gamma, \end{aligned} \tag{46}$$

which leads to

$$\begin{aligned}\sin\beta_{\rm out} &= \cos\omega_{\rm h}\sin\delta - \sin\omega_{\rm h}\cos\delta\cos\gamma \\ &= \cos\omega_{\rm h} Z - \sin\beta_{\rm in}(Y+1) \\ \Rightarrow Z &= [\sin\beta_{\rm out} + \sin\beta_{\rm in}(Y+1)]/\cos\omega_{\rm h}. \end{aligned} \quad (47)$$

Finally, with known Y and Z, we can solve for X:

$$\begin{aligned} h_\varphi^2 + k_\varphi^2 &= X^2 + (\cos\omega_{\rm h}\, Y + \sin\omega_{\rm h}\, Z)^2 \\ \Rightarrow X &= \pm[h_\varphi^2 + k_\varphi^2 - (\cos\beta_{\rm in}\, Y + \sin\beta_{\rm in}\, Z)^2]^{1/2}. \end{aligned} \quad (48)$$

Both the positive and negative solutions for X are valid, but often one may be preferred because of constraints in the mechanical setup. With the given choice of laboratory coordinates, a positive value of X would result in a γ rotation to negative angles (see Fig. 1). For our diffractometer setup, γ is constrained to small negative values, hence we choose the negative solution for X to ensure a γ rotation to positive angles.

Next, we solve for the diffractometer angles γ, δ, φ and ω_h. From equation (43), we obtain

$$\tan\gamma = \frac{\sin\gamma}{\cos\gamma} = \frac{-X}{Y+1} \quad (49)$$

and

$$\tan\delta = \frac{Z\sin\gamma}{-X}. \quad (50)$$

Note again that the tangent depends on the individual signs of the numerator and denominator, hence the need to use a quadrant-specific arctangent function (`atan2` in standard C).

Using the same method as in equations (29)–(32), we can find φ:

$$\tan\varphi = \frac{h_\varphi M - k_\varphi X}{h_\varphi X + k_\varphi M}, \quad (51)$$

where $M = \cos\beta_{\rm in}\, Y + \sin\beta_{\rm in}\, Z$.

Finally, $\omega_{\rm h}$ is simply equal to the incoming angle $\beta_{\rm in}$:

$$\sin\omega_{\rm h} = \sin\beta_{\rm in}. \quad (52)$$

The three constraints for the incoming and outgoing angles now result in the following relations:

(a) Fixed incoming angle $\beta_{\rm in}$:

$$\sin\beta_{\rm out} = l_\varphi - \sin\omega_{\rm h}. \quad (53)$$

(b) Fixed outgoing angle $\beta_{\rm out}$:

$$\sin\omega_{\rm h} = \sin\beta_{\rm in} = l_\varphi - \sin\beta_{\rm out}. \quad (54)$$

(c) Equal incoming and outgoing angles $\beta_{\rm in} = \beta_{\rm out}$:

$$\sin\beta_{\rm in} = \sin\beta_{\rm out} = l_\varphi/2. \quad (55)$$

4. Using the detector rotation

So far, we have neglected the detector rotation around the ν axis, as this has no effect on the positioning of a detector with its active area centred on this axis, and therefore does not affect the conversion from reciprocal-space coordinates to the other diffractometer angles and *vice versa*.

The original design idea for implementing the ν axis was to merge the properties of the z-axis- and (2+2)-type geometries (Vlieg, 1998). In particular, the ν-axis rotation offers the possibility of keeping the orientation of the detector slits aligned with the direction of the perpendicular scattering vector component $\mathbf{q}_\perp$, as shown in Fig. 3(a). When using rocking scans to integrate the diffraction signal for a particular value of $\mathbf{q}_\perp$, this slit orientation ensures a well defined acceptance $\Delta\mathbf{q}_\perp$ and leads to a simple correction factor for the amount of intercepted rod. The following calculation of the required rotation in ν has been presented by Vlieg (1998).

For both geometries, the ν-axis rotation is described by the following matrix (in both cases, ν rotates around the positive y axis):

$$N = \mathcal{R}_y(\nu) = \begin{pmatrix} \cos\nu & 0 & \sin\nu \\ 0 & 1 & 0 \\ -\sin\nu & 0 & \cos\nu \end{pmatrix}. \quad (56)$$

In the vertical geometry, at all angles zero, let $\hat{\mathbf{x}}_\nu$ and $\hat{\mathbf{z}}_\nu$ be two unit vectors in a coordinate system attached to the ν axis, which are aligned with the x and z axes of the laboratory frame of reference, respectively. Further, we will assume that the vertical and horizontal guard slit pairs are also aligned with the laboratory coordinate system and therefore move along the directions of $\hat{\mathbf{x}}_\nu$ and $\hat{\mathbf{z}}_\nu$.

The condition that the horizontal slits are aligned parallel with respect to $\mathbf{q}_\perp$ implies that $\hat{\mathbf{x}}_\nu$ is always perpendicular to the latter:

$$\hat{\mathbf{x}}_\nu \cdot \mathbf{q}_\perp = 0. \quad (57)$$

With all angles at zero, we have in the laboratory frame of reference

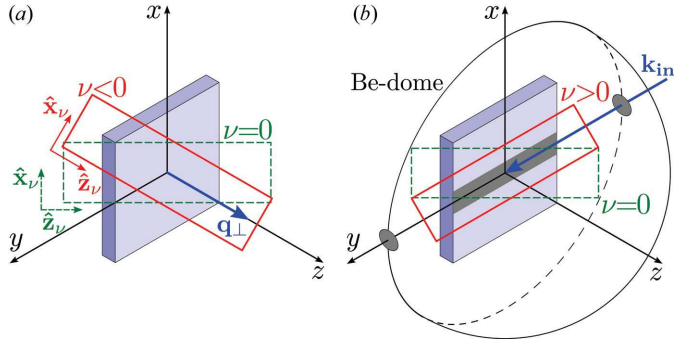

Figure 3
Two modes for the ν-axis rotation. (a) The guard slits and detector are aligned with the direction of $\mathbf{q}_\perp$ by rotating ν to negative values. (b) A rotation to positive ν values keeps the projection of the beam footprint (grey parallelogram) on the sample aligned with the slits and detector pixels and helps to effectively mask out scattering caused by the incoming X-rays upstream or downstream of the sample (grey discs). The sample is shown with all angles set to zero in both panels and the detector/slit orientation is indicated by the rectangle before (green, or dashed line in the print version of the paper) and after (red, or solid line in the print version of the paper) the rotation. See text for more details.

$$\mathbf{q}_\perp = q_z \begin{pmatrix} 0 \\ 0 \\ 1 \end{pmatrix}, \qquad \hat{\mathbf{x}}_\nu = \begin{pmatrix} 1 \\ 0 \\ 0 \end{pmatrix}, \tag{58}$$

where q_z is the perpendicular scattering vector component.

For non-zero angles, equation (57) becomes

$$(\Gamma \times \Delta \times N \times \hat{\mathbf{x}}_\nu)(A \times \mathbf{q}_\perp) = 0, \tag{59}$$

and can be solved to yield

$$\tan \nu = -\tan(\gamma - \alpha) \sin \delta. \tag{60}$$

Using the same procedure for the horizontal geometry, one finds

$$\tan \nu = \frac{-\sin \gamma \sin \omega_h}{\sin \omega_h \cos \gamma \sin \delta + \cos \omega_h \cos \delta}. \tag{61}$$

When using an area detector, however, there is a second mode of operation for the ν-axis rotation which proves very useful in many cases. Rather than keeping the detector and slits aligned with the $\mathbf{q}_\perp$ direction, it may be advantageous to align them with respect to the projection of the incoming X-ray beam, especially when working in the open-slit geometry in a stationary mode (Specht & Walker, 1993; Vlieg, 1997; Schlepütz *et al.*, 2005). This situation is depicted in Fig. 3(*b*). The relatively broad beam produced by a wiggler insertion device typically floods the entire sample length at grazing incoming angles, unless its width is significantly reduced by inserting a narrow aperture upstream of the sample. The scattering signal produced by a flooded sample, however, will result in an extended signal on the detector, where the extent is given by the projection of the beam footprint on the sample onto the detector. Fig. 4 shows two examples of this. For a fixed value of ν, the orientation of this extended signal on the detector depends on the detector angles (for example, the projected footprint rotates on the detector in a scan along the l direction).

There are two fundamental advantages in keeping the detector and slits aligned with the projected footprint direction: (i) the orientation of the signal on the detector will not change, which greatly facilitates data analysis and background removal, and (ii) the slit edges are aligned with the approximately rectangular signal shape, providing for the tightest possible slit aperture while ensuring that the entire signal is nonetheless integrated.

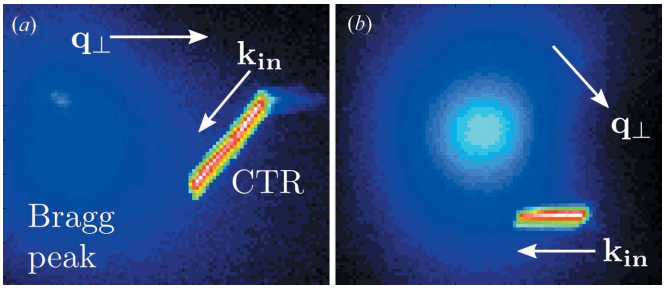

Figure 4
Detector images showing the crystal truncation rod signal acquired from a $NdGaO_3$ surface (sharp and intense elongated feature) close to a Bragg peak (broad diffuse feature) using the two different modes for the ν-axis rotation: (*a*) keeping the $\mathbf{q}_\perp$ direction aligned with the slits, and (*b*) keeping the direction of the beam footprint on the sample horizontal on the detector.

Another frequently encountered problem arises when using a sample environment such as an ultra-high-vacuum chamber with beryllium windows. The incident X-ray beam generates unwanted scattering where it penetrates the container walls (as shown by the yellow discs in Fig. 3*b*). These scattering sources are spatially separated from the sample along the direction of the incoming beam. Having the slits aligned along the $\mathbf{k}_{in}$ direction allows one to cut out this background scattering without the risk of blocking the signal from the sample at the same time. As the projected footprint size and the distance from the sample to the container walls change as a function of the detector position, the slit sizes may have to be adjusted dynamically for this mode.

Note that, for small incoming angles, the orientations of the footprint and the incoming X-ray beam are nearly identical, such that all of the above-mentioned advantages apply. The calculation for these modes is analogous to that for a stationary $\mathbf{q}_\perp$ direction previously. Now we require that either $\mathbf{k}_{in}$ or the direction of the footprint, which is given by $A \times \mathbf{k}_{in}$ in the vertical geometry, are perpendicular to the $\hat{\mathbf{x}}_\nu$ direction. For all angles equal to zero, this gives

$$\hat{\mathbf{x}}_\nu \cdot \mathbf{k}_{in} = 0. \tag{62}$$

At non-zero positions, equation (62) becomes

$$(\Gamma \times \Delta \times N \times \hat{\mathbf{x}}_\nu)(A \times \mathbf{k}_{in}) = 0, \tag{63}$$

and its solution is

$$\tan \nu = \frac{\sin \delta}{\tan(\gamma - \alpha)}. \tag{64}$$

Setting α to zero in equation (64) aligns the slits and detector with $\mathbf{k}_{in}$, while using the actual value of α keeps a constant orientation of the beam footprint.

Owing to the change in coordinate system, for the horizontal geometry we want to keep $\hat{\mathbf{x}}_\nu$ perpendicular to $\mathbf{k}_{in}$ (this will keep the same pairs of slits perpendicular or parallel to the footprint as for the vertical geometry), and we have to use the Ω_h rotation to take into account the incoming angle onto the surface:

$$(\Gamma \times \Delta \times N \times \hat{\mathbf{z}}_\nu)(\Omega_h \times \mathbf{k}_{in}) = 0, \tag{65}$$

which leads to

$$\tan \nu = \frac{\sin(\delta - \omega_h)}{\tan(\gamma)}. \tag{66}$$

Setting ω_h to zero again gives the correct orientation with respect to the incoming X-ray beam.

5. Calculating the reciprocal-space coordinates for each pixel

The observed direction of the outgoing scattering vector is different for each pixel on an area detector, resulting in a two-dimensional spatially resolved diffraction signal. We will now

discuss the conversion from pixel coordinates (i, j) to their corresponding hkl values and the appropriate intensity corrections to be applied to each pixel.

Consider Fig. 5(a). We assume that the detector has been mounted for normal incidence of the radiation onto its active area at some distance R from the diffractometer centre (DC), meaning that the directions of the pixel rows and columns (i, j) are perpendicular to the direction of $\mathbf{k}_{\rm out}$ and the detector rotation axis ν. With all detector angles set to zero ($\gamma = \delta = \nu = 0$), the direct X-ray beam hits the area detector at the nominal zero position on the detector (c_i, c_j), measured in units of pixels. (Note that c_i and c_j do not have to be integers. The beam position is normally calculated as the centre of mass of the incident intensity distribution, yielding a more accurate position.)

Using the coordinate system for the vertical geometry, a pixel at coordinate (i, j) is located at some offset $(\Delta x, \Delta z)$ from the direct-beam position:

$$\Delta x = (c_i - i)w_x, \quad \Delta z = (c_j - j)w_z, \tag{67}$$

where w_x and w_z are the pixel sizes along the x and z directions, respectively (for the PILATUS 100K, $w_x = w_z =$ 172 µm).

The $(x_{\rm p}, y_{\rm p}, z_{\rm p})$ position of this pixel in the laboratory frame of reference for non-zero detector angles can then be computed as

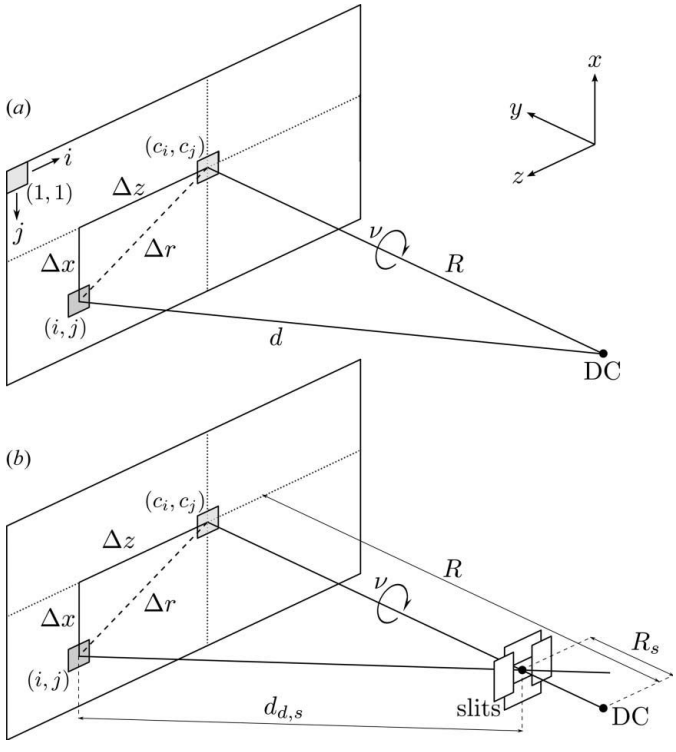

Figure 5
On the conversion from pixel coordinates to angular positions. (a) In the open-slit geometry, the angular offsets of non-centred pixels are determined by the distance R between the rotation centre and the detector and the linear offsets Δx, Δz in the plane of the detector. (b) When using resolution-defining slits, R needs to be replaced by the distance between the slits and the detector, given by $R - R_{\rm s}$.

$$\begin{pmatrix} x_{\rm p} \\ y_{\rm p} \\ z_{\rm p} \end{pmatrix} = \Gamma \times \Delta \times N \begin{pmatrix} \Delta x \\ R \\ \Delta z \end{pmatrix} \tag{68}$$

where Γ, Δ and N are the rotation matrices given in equations (8), (10) and (56), evaluated for the nominal detector angles.

Now there are two cases to be considered regarding the use of guard slits. Firstly, when using an open-slit geometry in a stationary mode (Specht & Walker, 1993; Vlieg, 1997; Schlepütz *et al.*, 2005), where the entire sample is visible by each pixel, the effective detector angles $\gamma_{\rm p}$ and $\delta_{\rm p}$ for each pixel are determined by (see Fig. 6a)

$$\gamma_{\rm p} = \arctan(z_{\rm p}/y_{\rm p}), \tag{69}$$

$$\delta_{\rm p} = \arcsin(x_{\rm p}/d), \tag{70}$$

where

$$d = [(\Delta x)^2 + R^2 + (\Delta z)^2]^{1/2} \tag{71}$$

is the actual distance of the pixel from the DC. (Note that the values of $\gamma_{\rm p}$ and $\delta_{\rm p}$ are independent of the choice of coordinate system. The exact same answer would have been obtained by using the horizontal geometry coordinate system.)

The second case, when using the guard slits to define the angular resolution of the measurement, is more complex. This is shown schematically in Fig. 5(b). The effective angles are no longer defined through the distance of the detector from the sample, but rather from the beam-defining aperture formed by the guard slits. Note that this also implies that the X-rays arriving at the pixel (i, j) are no longer originating at the DC, but from a point with a trajectory through the slits onto this pixel.

The calculations require a precise knowledge of the slit distance $R_{\rm s}$ from the DC. Rotating the detector also rotates the slit aperture in the laboratory frame of reference to a new position given by

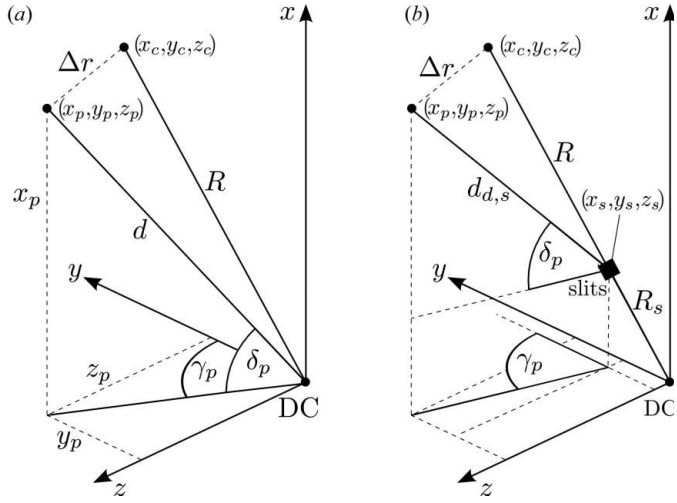

Figure 6
Calculating the effective detector angles $\gamma_{\rm p}$ and $\delta_{\rm p}$ for each detector pixel for (a) the open-slit geometry, and (b) using resolution-defining slits.

$$\begin{pmatrix} x_s \\ y_s \\ z_s \end{pmatrix} = \Gamma \times \Delta \begin{pmatrix} 0 \\ R_s \\ 0 \end{pmatrix}, \tag{72}$$

as shown in Fig. 6(*b*). Here we have assumed the slit aperture to be centred on the ν axis, which therefore does not need to be included in the transformation. The effective detector angles are then

$$\gamma_p = \arctan\left(\frac{z_p - z_s}{y_p - y_s}\right), \tag{73}$$

$$\delta_p = \arcsin\left(\frac{x_p - x_s}{d_{d,s}}\right), \tag{74}$$

where $d_{d,s}$ is the distance between the pixel and the slit aperture:

$$d_{d,s} = [(x_d - x_s)^2 + (y_d - y_s)^2 + (z_d - z_s)^2]^{1/2}. \tag{75}$$

It should be noted that calculating the angular offsets $\Delta\gamma$ and $\Delta\delta$ of each pixel from the nominal γ and δ positions by writing (for $\nu = 0$, see Fig. 5)

$$\Delta\gamma = \arctan\left(\frac{\Delta z}{R}\right), \quad \Delta\delta = \arctan\left(\frac{\Delta x}{R}\right) \tag{76}$$

is an approximation that is only valid for $R \gg \{\Delta x, \Delta z\}$ and $\gamma \simeq \delta \simeq 0$. It relies on the assumption that a change (Δz) in the pixel position results in a certain change in γ independent of δ. In general, however, the mapping of the spherical (γ, δ) coordinates onto the Cartesian detector coordinates is more complex, as is illustrated in Fig. 7, and the results from equations (69) and (70) or (73) and (74) have to be used.

Knowing the effective angular positions for each pixel now (the sample angles are independent of pixel position and hence identical for all pixels), the corresponding *hkl* values can be computed straightforwardly by combining equations (13) and (15) for the vertical geometry, or equations (43) and (44) for the horizontal geometry, to calculate $H_{\varphi/\omega}$. Multiplying by the inverse of the orientation matrix then yields the *hkl* values in the crystal frame of reference:

$$\mathbf{H} = (UB)^{-1}\,\mathbf{H}_{\varphi/\omega}. \tag{77}$$

The intensities measured in each pixel need to be corrected with the usual correction factors (Vlieg, 1997; Schlepütz *et al.*, 2005), most of which depend on γ or δ and therefore have to be calculated individually.

If slits are used to define the active scattering area on the sample surface, the active area correction also has to be calculated with respect to each pixel location. A ray-tracing approach to this problem has been presented by Mariager, Lauridsen *et al.* (2009).

In addition to these standard corrections, the relative change in solid scattering angle for the different pixels has to be taken into account. Owing to the flat detector surface, pixels away from the direct-beam position will be (i) further away from the DC, and (ii) at non-normal incidence with respect to the scattered beam, both of which result in a decrease of the subtended solid angle.

For the open-slit geometry, the change in distance is taken into account by multiplying each pixel's integrated intensity by a correction factor of

$$C_d = d^2/R^2, \tag{78}$$

while the change in projected pixel size due to the beam inclination is compensated for by

$$C_i = 1/\cos[\arctan(\Delta r/R)], \tag{79}$$

with $\Delta r = [(\Delta x)^2 + (\Delta z)^2]^{1/2}$ (see Fig. 5).

With closed slits, the inclination correction is modified in the following way:

$$C_i = 1/\cos\{\arctan[\Delta r/(R - R_s)]\}. \tag{80}$$

The change in distance, however, also depends on the orientation of the sample since different parts of the sample surface are visible to different pixels. Also, here, the ray-tracing approach (Mariager, Lauridsen *et al.*, 2009) can be used to calculate the effective sample-to-detector distance d' for all pixels, yielding a correction factor of

$$C_d = d'^2/R^2. \tag{81}$$

Note that the corrections by C_i and C_d become negligible when the extent of the detector's active area is much smaller than the sample-to-detector distance ($R \gg \Delta r$), which is normally the case. For example, using R = 1140.8 mm and assuming the nominal zero position of the detector is exactly in its centre, the largest necessary corrections occur for the corner pixels of the PILATUS 100K and have values of

$$C_d = 1.0016, \qquad C_i = 1.00078, \tag{82}$$

in the open-slit case.

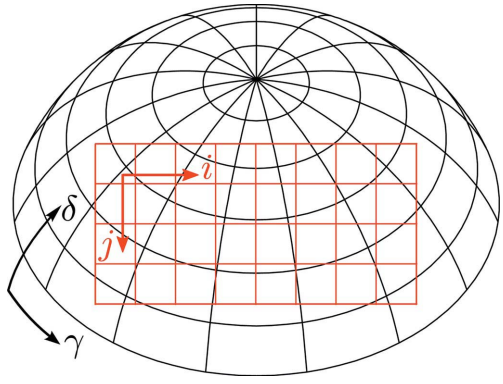

Figure 7
On the conversion from polar detector angle coordinates $\{\gamma, \delta\}$ to Cartesian pixel coordinates $\{i, j\}$. Changing only one coordinate in one system generally results in a change of both coordinate values in the other system.

6. Recording three-dimensional RSMs

The mapping of pixel coordinates to *hkl* values corresponds to a curved slice through reciprocal space, which is given by all

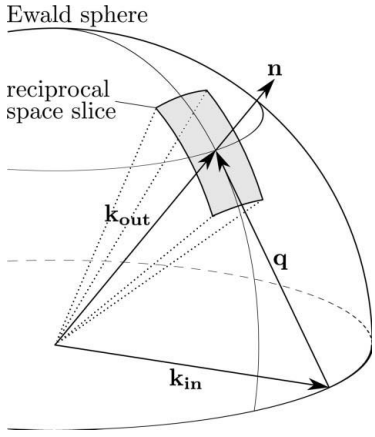

Figure 8
The diffraction signal observed by an area detector corresponds to a curved slice in reciprocal space, given by the portion of the Ewald sphere that is visible by the detector. To produce three-dimensional reciprocal-space maps, it is best to record a set of such slices which are offset with respect to each other along the direction perpendicular to the slice surfaces. This normal direction **n** is identical to the direction of $\mathbf{k}_{out}$.

those reciprocal-space points lying on the surface of the Ewald sphere that are visible by the detector (see Fig. 8). The optimal sampling of reciprocal space to obtain a three-dimensional RSM is achieved by recording a set of these slices along the normal direction **n** to the slice surfaces (Mariager, Lauridsen *et al.*, 2009). As can be seen in Fig. 8, this is equal to the direction of $\mathbf{k}_{out}$.

In order to perform a reciprocal-space scan along this direction, we must express $\mathbf{k}_{out}$ in terms of the reciprocal-lattice coordinates of the crystal. Using the results from §3, we can rewrite the scattering condition, $\mathbf{k}_{out} = \mathbf{k}_{in} + \mathbf{q}$. We transform the known direction of the incoming X-ray beam, $\mathbf{k}_{in}$, from the laboratory frame of reference to reciprocal-space coordinates. Then, for a specific scattering vector **q**, given in reciprocal space by $\mathbf{H} = (h, k, l)$, $\mathbf{k}_{out}$ becomes

$$\mathbf{k}_{out,latt} = (UB)^{-1}\Omega_v^{-1}A^{-1}\begin{pmatrix}0\\1\\0\end{pmatrix} + \begin{pmatrix}h\\k\\l\end{pmatrix}. \qquad (83)$$

An example of a three-dimensional RSM obtained from a single area-detector scan is shown in Fig. 9. The data were measured on a sample with GaAs nanowires grown on a GaAs substrate. The scattering intensity distribution around the GaAs zincblende $[11\bar{1}]$ Bragg peak has been obtained using the reciprocal-space coordinate calculations derived in §5. A detailed description of this system can be found in Mariager *et al.* (2007) and Mariager, Schlepütz *et al.* (2009).

7. Conclusion

The angle calculations for a (2+3)-type surface diffractometer have been detailed in a comprehensive, step-by-step manner, both for the horizontal and for the vertical scattering geometry. They are a direct adaptation from the original calculations for the (2+2)-type diffractometer by Evans-Lutterodt & Tang (1995) and the (2+3)-type design by Vlieg (1998), and establish a firm basis for the discussion of some particular aspects of using area detectors. Firstly, a new mode for the detector rotation particularly suited to the use of area detectors, in which the orientation of the detector and the detector slits is aligned with the incoming X-ray beam, has been described. Secondly, we have focused on obtaining two-dimensional reciprocal-space maps from single detector images. The presented formalism to convert between pixel positions and reciprocal-space coordinates is independent of a particular diffractometer geometry, and hence generally applicable.

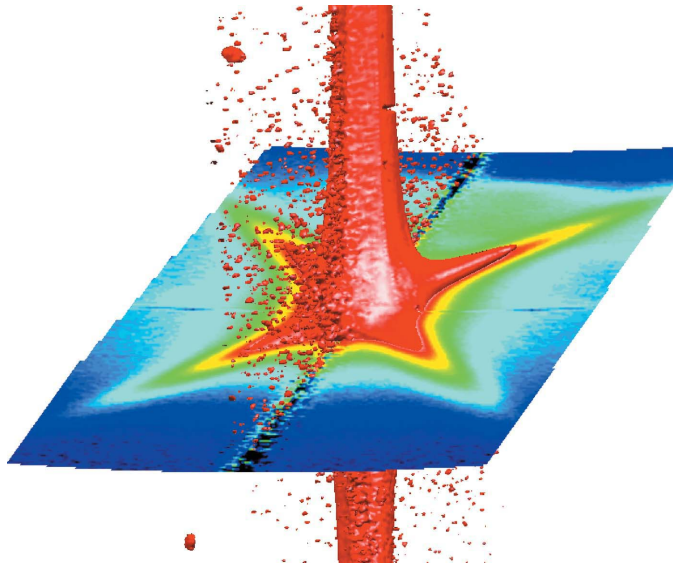

Figure 9
Example of a three-dimensional reciprocal-space map recorded from a sample of GaAs nanowires grown on GaAs. The volume data set around the zincblende $[11\bar{1}]$ Bragg peak is visualized through a three-dimensional isosurface (red) and an oblique slice through reciprocal space. The strong vertical feature is the substrate crystal truncation rod and the signal within the slice plane originates from the nanowire facet truncation rods (Mariager *et al.*, 2007; Mariager, Schlepütz *et al.*, 2009).

The authors would like to thank Christian Brönnimann, Beat Henrich, Philipp Kraft, Eric Eikenberry, Oliver Bunk, Roger Herger, Domenico Martoccia and Matts Björck for their technical and experimental assistance and valuable discussions. Support of this work by the Schweizerischer Nationalfonds zur Förderung der wissenschaftlichen Forschung and the staff of the Swiss Light Source is gratefully acknowledged. Parts of this work were also funded by the Danish Natural Science Council through DANSCATT. This work was performed at the Swiss Light Source, Paul Scherrer Institut, Switzerland.

References

Bergamaschi, A., Brönnimann, C., Eikenberry, E. F., Henrich, B., Kobas, M., Kraft, P. & Schmitt, B. (2007). *Proc. Sci.* **57**, 49.
Bloch, J. M. (1985). *J. Appl. Cryst.* **18**, 33–36.
Bunk, O. & Nielsen, M. M. (2004). *J. Appl. Cryst.* **37**, 216–222.
Busing, W. R. & Levy, H. A. (1967). *Acta Cryst.* **22**, 457–464.

Clegg, W. (1984). *Acta Cryst.* A**40**, 703–704.
Evans-Lutterodt, K. W. & Tang, M. T. (1995). *J. Appl. Cryst.* **28**, 318–326.
Hung, H.-H. (1992). *J. Appl. Cryst.* **25**, 761–765.
Kraft, P., Bergamaschi, A., Broennimann, Ch., Dinapoli, R., Eikenberry, E. F., Henrich, B., Johnson, I., Mozzanica, A., Schlepütz, C. M., Willmott, P. R. & Schmitt, B. (2009). *J. Synchrotron Rad.* **16**, 368–375.
Kraft, P., Bergamaschi, A., Brönnimann, C., Dinapoli, R., Eikenberry, E. F., Graafsma, H., Henrich, B., Johnson, I., Kobas, M., Mozzanica, A., Schlepütz, C. M. & Schmitt, B. (2009). *IEEE Trans. Nucl. Sci.* **56**, 758–764.
Lohmeier, M. & Vlieg, E. (1993). *J. Appl. Cryst.* **26**, 706–716.
Mackay, A. L. (1984). *Acta Cryst.* A**40**, 165–166.
Mariager, S. O., Lauridsen, S. L., Dohn, A., Bovet, N., Sørensen, C. B., Schlepütz, C. M., Willmott, P. R. & Feidenhans'l, R. (2009). *J. Appl. Cryst.* **42**, 369–375.
Mariager, S. O., Schlepütz, C. M., Aagesen, M., Sørensen, C. B., Johnson, E., Willmott, P. R. & Feidenhans'l, R. (2009). *Phys. Status Solidi A*, **206**, 1771–1774.
Mariager, S. O., Sørensen, C. B., Aagesen, M., Nygard, J., Feidenhans'l, R. & Willmott, P. R. (2007). *Appl. Phys. Lett.* **91**, 083106.
Ralph, R. L. & Finger, L. W. (1982). *J. Appl. Cryst.* **15**, 537–539.
Renaud, G., Villette, B. & Guénard, P. (1995). *Nucl. Instrum. Methods Phys. Res. Sect. B*, **95**, 422–430.
Schlepütz, C. M., Herger, R., Willmott, P. R., Patterson, B. D., Bunk, O., Brönnimann, Ch., Henrich, B., Hülsen, G. & Eikenberry, E. F. (2005). *Acta Cryst.* A**61**, 418–425.
Schmidbauer, M., Schäfer, P., Besedin, S., Grigoriev, D., Köhler, R. & Hanke, M. (2008). *J. Synchrotron Rad.* **15**, 549–557.
Shoemaker, D. P. (1970). *J. Appl. Cryst.* **3**, 179–180.
Shoemaker, D. P. & Bassi, G. (1970). *Acta Cryst.* A**26**, 97–101.
Sobott, B. A., Broennimann, Ch., Eikenberry, E. F., Dinapoli, R., Kraft, P., Taylor, G. N., Willmott, P. R., Schlepütz, C. M. & Rassool, R. P. (2009). *J. Synchrotron Rad.* **16**, 489–493.
Specht, E. D. & Walker, F. J. (1993). *J. Appl. Cryst.* **26**, 166–171.
Takahasi, M. & Mizuki, J. (1998). *J. Synchrotron Rad.* **5**, 893–895.
Vlieg, E. (1997). *J. Appl. Cryst.* **30**, 532–543.
Vlieg, E. (1998). *J. Appl. Cryst.* **31**, 198–203.
You, H. (1999). *J. Appl. Cryst.* **32**, 614–623.